CO survey of high-z radio galaxies, revisited with ALMA: Jet-cloud Alignments and Synchrotron Brightening by Molecular Gas in the Circumgalactic Environment

Bjorn Emonts, Matthew Lehnert, Sophie Lebowitz, George K Miley, Montserrat Villar-Martin, Ray Norris, Carlos de Breuck, Chris Carilli, Ilana Feain

The Astrophysical Journal, 952:148 (14pp), 2023 August 1 https://doi.org/10.3847/1538-4357/acde53

CO Survey of High-z Radio Galaxies, Revisited with the Atacama Large Millimeter/submillimeter Array: Jet–Cloud Alignments and Synchrotron Brightening by Molecular Gas in the Circumgalactic Environment

Bjorn H. C. Emonts[1], Matthew D. Lehnert[2], Sophie Lebowitz[3,4], George K. Miley[5], Montserrat Villar-Martín[6], Ray Norris[7,8], Carlos De Breuck[9], Chris Carilli[10], and Ilana Feain[11]

[1] National Radio Astronomy Observatory, 520 Edgemont Road, Charlottesville, VA 22903, USA; bemonts@nrao.edu
[2] Université Lyon 1, ENS de Lyon, CNRS UMR5574, Centre de Recherche Astrophysique de Lyon, F-69230 Saint-Genis-Laval, France
[3] Steward Observatory, Department of Astronomy, University of Arizona, 993 North Cherry Avenue, Tucson, AZ 85721, USA
[4] Department of Astronomy, The Ohio State University, Columbus, OH 43210, USA
[5] Leiden Observatory, Leiden University, PO Box 9513, 2300 RA Leiden, The Netherlands
[6] Centro de Astrobiología, CSIC-INTA, Ctra. de Torrejón a Ajalvir, km 4, E-28850 Torrejón de Ardoz, Madrid, Spain
[7] CSIRO Space & Astronomy, P.O. Box 76, Epping, NSW 1710, Australia
[8] School of Science, Western Sydney University, Locked Bag 1797, Penrith, NSW 2751, Australia
[9] European Southern Observatory, Karl Schwarzschild Strasse 2, D-85748 Garching bei München, Germany
[10] National Radio Astronomy Observatory, P.O. Box O, Socorro, NM 87801, USA
[11] Quasar Satellite Technologies PTY Ltd, Cnr Vimiera and Pembroke Roads, Marsfield, NSW 2122, Australia
Received 2023 April 21; revised 2023 June 2; accepted 2023 June 12; published 2023 July 26

Abstract

Powerful radio sources associated with supermassive black holes are among the most luminous objects in the universe, and are frequently recognized both as cosmological probes and active constituents in the evolution of galaxies. We present alignments between radio jets and cold molecular gas in the environment of distant radio galaxies, and show that the brightness of the radio synchrotron source can be enhanced by its interplay with the molecular gas. Our work is based on CO $J > 1$ observations with the Atacama Large Millimeter/submillimeter Array (ALMA) of three radio galaxies with redshifts in the range $1.4 < z < 2.1$, namely MRC 0114-211 ($z = 1.41$), MRC 0156-252 ($z = 2.02$), and MRC 2048-272 ($z = 2.05$). These ALMA observations support previous work that found molecular gas out to 50 kpc in the circumgalactic environment, based on a CO(1–0) survey performed with the Australia Telescope Compact Array. The CO emission is found along the radio axes but beyond the main radio lobes. When compared to a large sample of high-z radio galaxies from the literature, we find that the presence of this cold molecular medium correlates with an increased flux-density ratio of the main versus counter-lobe. This suggest that the radio lobe brightens when encountering cold molecular gas in the environment. While part of the molecular gas is likely related to the interstellar medium from either the host or a companion galaxy, a significant fraction of the molecular gas in these systems shows very low excitation, with $r_{2-1/1-0}$ and $r_{3-2/1-0}$ values $\lesssim$0.2. This could be part of the circumgalactic medium.

Unified Astronomy Thesaurus concepts: High-redshift galaxies (734); Radio galaxies (1343); Radio jets (1347); Radio loud quasars (1349); Ultraluminous infrared galaxies (1735); Galaxy environments (2029); Circumgalactic medium (1879); Radio astrometry (1337); Millimeter astronomy (1061); Submillimeter astronomy (1647); Intracluster medium (858); Protoclusters (1297)

1. Introduction

High-z radio galaxies are among the most massive and active systems in the early universe (Miley & De Breuck 2008). They are key objects for better understanding a range of astrophysical phenomena, from black hole activity to galaxy and cluster formation (e.g., Pentericci et al. 2001; Vernet et al. 2001; Kurk 2003; Smail et al. 2003; Stevens et al. 2003; Rocca-Volmerange et al. 2004; Overzier 2006; Kodama et al. 2007; Seymour et al. 2007; Villar-Martín et al. 2007a; De Breuck et al. 2010; Barthel et al. 2012; Galametz et al. 2012; Wylezalek et al. 2013; Dannerbauer et al. 2014; Falkendal et al. 2019). High-z radio galaxies at $z > 1$ are typically defined as having a radio luminosity at 500 MHz in the rest frame of $L_{500} > 10^{27.5}$ W Hz^{-1} (Miley & De Breuck 2008). Their bright radio sources originate from the accretion-disk region around a supermassive black hole, where biconical magnetic fields accelerate charged particles that emit synchrotron radiation (see reviews by Miley 1980 and Blandford 2001). This process creates radio jets and lobes, which can propagate well beyond the host galaxy and are often hundreds of kiloparsecs in size (e.g., Carilli et al. 1997; Barthel et al. 2000; Pentericci et al. 2000).

Because their bright radio continuum is easily detectable, high-z radio galaxies have long acted as beacons for tracing distant galaxies (e.g., Roettgering et al. 1994, 1997; De Breuck et al. 2000; Saxena et al. 2018; Broderick et al. 2022). Therefore, high-z radio galaxies were among the first laboratories for studying galaxy formation in the early universe (e.g., Spinrad et al. 1981; McCarthy et al. 1987a, 1990; Chambers et al. 1990). Deep follow-up optical and infrared imaging and spectroscopy showed that their hosts are massive galaxies at redshifts of $z \sim 2$–5 (see review by McCarthy 1993; also Djorgovski et al. 1988; Lehnert et al. 1992; McCarthy et al. 1995; Chambers et al. 1996, 1996; Stern et al. 1999; De Breuck et al. 2001). In addition to being beacons for tracing

distant galaxies, the powerful high-z radio sources also play a key role in the formation and evolution of galaxies and galaxy clusters, for example, by driving massive outflows of gas (Nesvadba et al. 2017). Intriguing "alignment effects" have also been observed between the radio jets and various constituents of the radio host galaxy (Miley & De Breuck 2008). This includes alignments with the ultraviolet (UV) rest-frame continuum and submillimeter emission, which has been interpreted as jet-triggered star formation (Chambers et al. 1987; McCarthy et al. 1987b; Begelman & Cioffi 1989; De Young 1989; Rees 1989; Pentericci et al. 1999; Bicknell et al. 2000; Stevens et al. 2003; Ivison et al. 2012).

High-z radio galaxies were also among the first objects observed to contain a rich circumgalactic medium (CGM), primarily detected in the form of giant Lyα nebulae of ionized gas (McCarthy et al. 1987a; Chambers et al. 1990; Heckman et al. 1991; van Ojik et al. 1996; Villar-Martín et al. 2002, 2003, 2006, 2007b; Reuland et al. 2003, 2007; Miley et al. 2006; Humphrey et al. 2008; Swinbank et al. 2015; Vernet et al. 2017; Falkendal et al. 2021). These Lyα nebulae often show kinematically perturbed gas along the radio axis, with more quiescent gaseous halos detected beyond the extent of radio source (Villar-Martín et al. 2003; Humphrey et al. 2006). Ionized gas nebulae associated with high-z radio galaxies are also seen in Hα and are often enriched with heavy elements across tens of kiloparsecs (e.g., McCarthy et al. 1992; Carson et al. 2001; Kurk et al. 2002; Villar-Martín et al. 2003; Swinbank et al. 2015; Nesvadba et al. 2017; Falkendal et al. 2021). In some cases, cold molecular gas is found in the halo environment of high-z radio galaxies (Klamer et al. 2004, 2005; Ivison et al. 2012; Emonts et al. 2014, 2015a, 2016; Gullberg et al. 2016; Falkendal et al. 2021; Li et al. 2021; Wang et al. 2021; De Breuck et al. 2022).

Klamer et al. (2004) discovered that CO emission from cold molecular gas is often offset from the host galaxy and preferentially aligned along the radio axis. Other studies showed similar alignments between the radio source and cold molecular halo gas, including radio-loud quasars at $z\sim0.3$ (Aravena et al. 2011; Papadopoulos et al. 2008; Elbaz et al. 2009) and $z\sim2.2$ (Li et al. 2021), as well as the radio galaxies TXS 0828+193 at $z\sim2.6$ (Nesvadba et al. 2009; Fogasy et al. 2021) and TN J0924-2201 at $z\sim5.2$ (Lee et al. 2023). This alignment effect was also revealed by a CO(1–0) survey performed with the Australia Telescope Compact Array (ATCA; Emonts et al. 2014, hereafter Paper I).

The ATCA survey from Paper I utilized the ultracompact array configurations of the ATCA to obtain exquisite surface-brightness sensitivity for detecting CO(1–0) emission on scales of tens of kiloparsecs in a representative sample of high-z radio galaxies from the flux-limited 408 MHz Molonglo Reference (MRC) Catalogue (Large et al. 1981). This ATCA survey revealed that five out of 13 high-z radio galaxies in the sample (38%) contain detectable amounts of CO(1–0) in the halo environment, preferentially aligned along the radio axis. One of these systems, MRC 0152-209 (also known as the "Dragonfly Galaxy"), was observed with the Atacama Large Millimeter/submillimeter Array (ALMA) at high resolution in CO(6-5), which revealed that the radio jet aligns and interacts with molecular gas in the disk of a merging companion galaxy (Lebowitz et al. 2023). For three other systems observed as part of the ATCA survey, namely MRC 0114-211, MRC 0156-252, and MRC 2048-272, all of the CO(1–0) emission was detected in a single molecular gas reservoir, located beyond the brightest edge of the radio source. As shown in Paper I, even though the CO(1–0) luminosity of this halo gas is similar to what is typically found in submillimeter galaxies, the peaks of the CO(1–0) emission coincide with regions that are devoid of 4.5 μm infrared emission down to 1–2 mag below L^*, based on observations with the Infrared Array Camera (IRAC) Band 2 on the Spitzer Space Telescope (Galametz et al. 2012; Wylezalek et al. 2013).

This paper further investigates the molecular gas in the three high-z radio galaxies MRC 0114-211, MRC 0156-252, and MRC 2048-272, through CO(2–1) and CO(3–2) observations performed with ALMA. A comparison of the properties and spatial distributions between the CO-emitting gas and the radio synchrotron emission will be used to further study the observed alignments between radio sources and cold gas. The goal is to understand the nature of interaction between the radio source and molecular gas in the halos of high-z radio galaxies.

Throughout this paper, we shall assume the same cosmological parameters as in Paper I, namely $H_0=71$ km s^{-1} Mpc^{-1}, $\Omega_M=0.27$, and $\Omega_\lambda=0.73$ (Wright 2006).

2. Atacama Large Millimeter/submillimeter Array Data

MRC 0114-211 ($z=1.41$), MRC 0156-252 ($z=2.02$), and MRC 2048-272 ($z=2.05$) were observed with the 12 m ALMA and 7 m Atacama Compact Array (ACA) as part of ALMA Cycle 3 (ID: 2015.1.00897.S). We targeted the lowest transition of CO that is observable with ALMA, which for MRC 0114-211 is CO(2–1), and for MRC 0156-252 and MRC 2048-272 is CO(3–2), all covered in Band 3 (Claude et al. 2005). The ALMA 12 m array observed MRC 0114-211, MRC 0156-252, and MRC 2048-272 during 2016 January 12–19 in C36-1 configuration for 56, 138, and 111 minutes, respectively, which included time for slewing and calibration. The 7 m ACA observations were observed during 2016 January–September, with corresponding total observing times of 3.7, 9.4, and 7.6 hr, not including observations that failed ALMA's quality assurance process. We used four spectral windows of 1.875 GHz with 2 MHz channels. For MRC 0114-211 and MRC 0156-211, one of the spectral windows was centered around the redshifted CO line, while the remaining three covered line-free continuum emission. For MRC 2048-272, which had a wider overall CO(1–0) signal (Paper I), two of the four spectral windows were stitched together to cover the CO line, while the other two observed only continuum emission. A standard strategy for bandpass, phase, and flux calibration was adopted as part of the ALMA calibration plan.

The ALMA data were reduced with the Common Astronomy Software Applications (CASA; CASA Team et al. 2022). Calibration was performed with the scriptForPI.py calibration scripts that were included with the archival data set, using CASA v.4.5.1 with pipeline v.r35932 for the 12 m data of MRC 0114-211 and MRC 2048-272, CASA v.4.5.3 with pipeline r36115 for the 7 m data of MRC 0114-211, CASA v.4.6.0 (without pipeline) for the 12 m data of MRC 0156-252, and CASA v.4.7.0 with pipeline v.r38377 for the 7 m data of MRC 0156-252 and MRC 2048-272.

Images were made using CASA v.5.6.0. First, we subtracted the continuum emission using CASA task UVCONTSUB by fitting a straight line to the line-free channels for each visibility. We then imaged the continuum-subtracted line emission using CASA task TCLEAN, utilizing the MOSAIC gridder to combine

Table 1
ALMA CO Line Data Properties

Source MRC	CO(J, $J-1$) Transition	Beam Size (PA) (arcsecond^2)	ΔAstrometry[a] (arcseconds)	Channel Width (km s^{-1})	Spectral Resolution (km s^{-1})	rms Noise[b] (mJy bm^{-1} chan^{-1})
0114-211	$J=2$	3.47×2.43 ($-86.^\circ8$)	0.4	100	200	0.11
0156-252	$J=3$	3.04×2.00 ($74.^\circ1$)	0.3	60	120	0.21
2048-262	$J=3$	3.35×1.98 ($87.^\circ0$)	0.4	100	200	0.14

Notes.
[a] The astrometric uncertainty of the CO detections discussed in this paper is dominated by the limited signal-to-noise ratio (S/N), which results in small positional errors with respect to the phase center. This astrometric error is calculated using $\delta\theta_{\rm rms}=\frac{1}{2}\,\langle\Theta_{\rm beam}\rangle\,({\rm S/N})^{-1}$ (Papadopoulos et al. 2008). For values in this table, ΔAstrometry $\equiv\delta\theta_{\rm rms}$, and $\langle\Theta_{\rm beam}\rangle$ is the major axis of the beam size. An additional uncertainty in the absolute astrometry, due to phase errors introduced by errors in the baseline length, is calculated using $\delta\theta_{\rm bas}=(\delta\,\boldsymbol{B}\cdot\Delta\,\boldsymbol{k})/\,\boldsymbol{B}\approx(\delta\Phi_{\rm bas}/2\pi)\langle\Theta_{\rm beam}\rangle$ (Papadopoulos et al. 2008), with $\delta\Phi_{\rm bas}\sim(2\pi/\lambda)(\delta\boldsymbol{B}\cdot\Delta\boldsymbol{k})$, $\Delta\boldsymbol{k}$ is the distance to the phase calibrator, and $|\delta\boldsymbol{B}|$ is the calibration error of the baseline length. For ALMA, $|\delta\boldsymbol{B}|\sim0.2$ mm km^{-1} (Hunter et al. 2016), with maximum 12 m baselines in our data of $\lesssim$350 m, while for ATCA we assume $|\delta\boldsymbol{B}|\sim1$ mm. This means that $\Delta\theta_{\rm bas}\ll\delta\theta_{\rm rms}$ for the data presented in this paper.
[b] rms noise before primary beam correction and after Hanning smoothing.

the 12 m and 7 m data. We also performed a correction for the primary beam response. After binning the image cube to a channel width that best visualizes the line emission, we applied a Hanning smooth to optimize the CO signals. This Hanning smooth created an effective velocity resolution that is twice the channel width. Because of the faintness of the CO, no deconvolution was applied (but see Appendix A). Table 1 summarizes the spatial resolution (synthesized beam size), astrometric accuracy, spectral resolution, and rms noise level of the image products after combining the 12 m and 7 m data.

3. Results

3.1. ALMA Results

Figures 1–3 show the ALMA imaging of MRC 0114-211, MRC 0156-252, and MRC 2048-262. For all three sources, ALMA detects a $J>1$ transition of CO along the radio axis but beyond the outer edge of the radio source, near the location of the previous ATCA detections of CO(1–0) (Paper I).

1. *MRC 0114-211:* This target contains a small, compact steep spectrum (CSS) radio source with a length of ∼6 kpc (De Breuck et al. 2010; Randall et al. 2011). The reservoir of CO(1–0) was detected with the ATCA at 4.5σ significance, and found along the radio jet at a distance of 34 kpc from the center of the galaxy (Paper I). The estimated molecular gas mass is $M_{\rm H_2}=(4.5\pm0.9)\cdot\alpha_{\rm CO}\times10^{10}\,M_\odot$, with $\alpha_{\rm CO}=M_{\rm H2}/L'_{\rm CO}$ the CO conversion factor that translates the CO luminosity ($L'_{\rm CO}$) into $M_{\rm H2}$ (Bolatto et al. 2013), and which typically ranges from 0.8 for ultraluminous infrared galaxies (Downes & Solomon 1998) to 3.6 for high-z star-forming galaxies (Daddi et al. 2010; Genzel et al. 2010). Despite this large molecular gas mass, the region of the CO(1–0) emission is devoid of any emission in deep IRAC 4.5 μm imaging (Figure 1).

Our ALMA data show a CO(2–1) detection roughly $0.''8$ beyond the radio source, in between the bright radio hot spot and the previous CO(1–0) detection. The redshift of the CO(2–1) detection, $z=1.414\pm0.001$, is in good agreement with that derived from the optical [O III] and Hα lines (Nesvadba et al. 2017), but shifted by ∼1500 km s^{-1} with respect to the peak of the CO(1–0) detection. The molecular gas mass associated with this CO(2–1) detection is $M_{\rm H_2(comp)}<1.8\times10^{10}\cdot\alpha_{\rm CO}\,M_\odot$ (see Solomon & Vanden Bout 2005), where $\alpha_{\rm CO}$ is the CO-to-H$_2$ conversion factor (Bolatto et al. 2013). This estimate is based on the limit of $r_{2-1/1-0}$ given in Table 2.

2. *MRC 0156-252:* This target is associated with an extended radio source having a total linear size of ∼70 kpc and a spectacular 90° bend at its bright outer edge (Carilli et al. 1997). Luminous Lyα emission was found by Pentericci et al. (2001) to stretch along the radio axis, peaking at the location of the bright end of the radio source. The CO(1–0) emission observed with the ATCA at 5σ significance is found beyond the radio source, while a region with diffuse X-ray emission is seen to the north of it (Overzier et al. 2005). The CO(1–0) emission has a total mass of $M_{\rm H_2}\sim(7.4\pm1.5)\times10^{10}\cdot\alpha_{\rm CO}\,M_\odot$ (Paper I) and is resolved into two components, which are separated by approximately $3''$ and 900 km s^{-1} (regions B1 and B2 in Figure 2).

Our ALMA data show a clear CO(3–2) detection at a redshift of $z=2.025\pm0.001$ marked as region A in Figure 2, which is located close to the CO(1–0) component in region B1. This ALMA detection is cospatial with a faint infrared source in deep IRAC 4.5 μm imaging (Figure 2), and therefore likely represents the molecular interstellar medium (ISM) in a companion galaxy. This source was identified by Galametz et al. (2013) to be a red galaxy that is very faint in the optical and, hence, was not targeted by them for spectroscopic follow-up. Our ALMA data confirm that it is at about the same redshift as MRC 0156-252.

Component B2, which was detected only in CO(1–0), is located in the region between the radio host galaxy and the companion in region A. The CO(1–0) peaks southwest of another, much bluer companion galaxy, which is found at the approximate location of the radio hot spot (Galametz et al. 2013). This companion galaxy is not visible in Figure 2. The redshift of this second companion is $z=2.0171\pm0.0004$ as derived from He II, which differs by ∼300 km s^{-1} from the CO(1–0) velocity of the emission-line peak of component B2 (Figure 2). The CO(1–0) emission in region B2 may originate from this companion, or be a CGM component.

We also detect the host galaxy of MRC 0156-252 in CO(3–2) at $z=2.024\pm0.001$, which is close to the redshift derived from He II of $z=2.0256\pm0.0002$ (Galametz et al. 2013). There is a slight offset between the radio core and the peak of the central CO(3–2) emission, which lies ∼$1''$ to the east, along the direction of the counter-jet. However, we cannot confirm that this offset is real, due to the uncertainties in the astrometry of the ALMA and radio continuum images, in particular because self-calibration of the Very Large Array

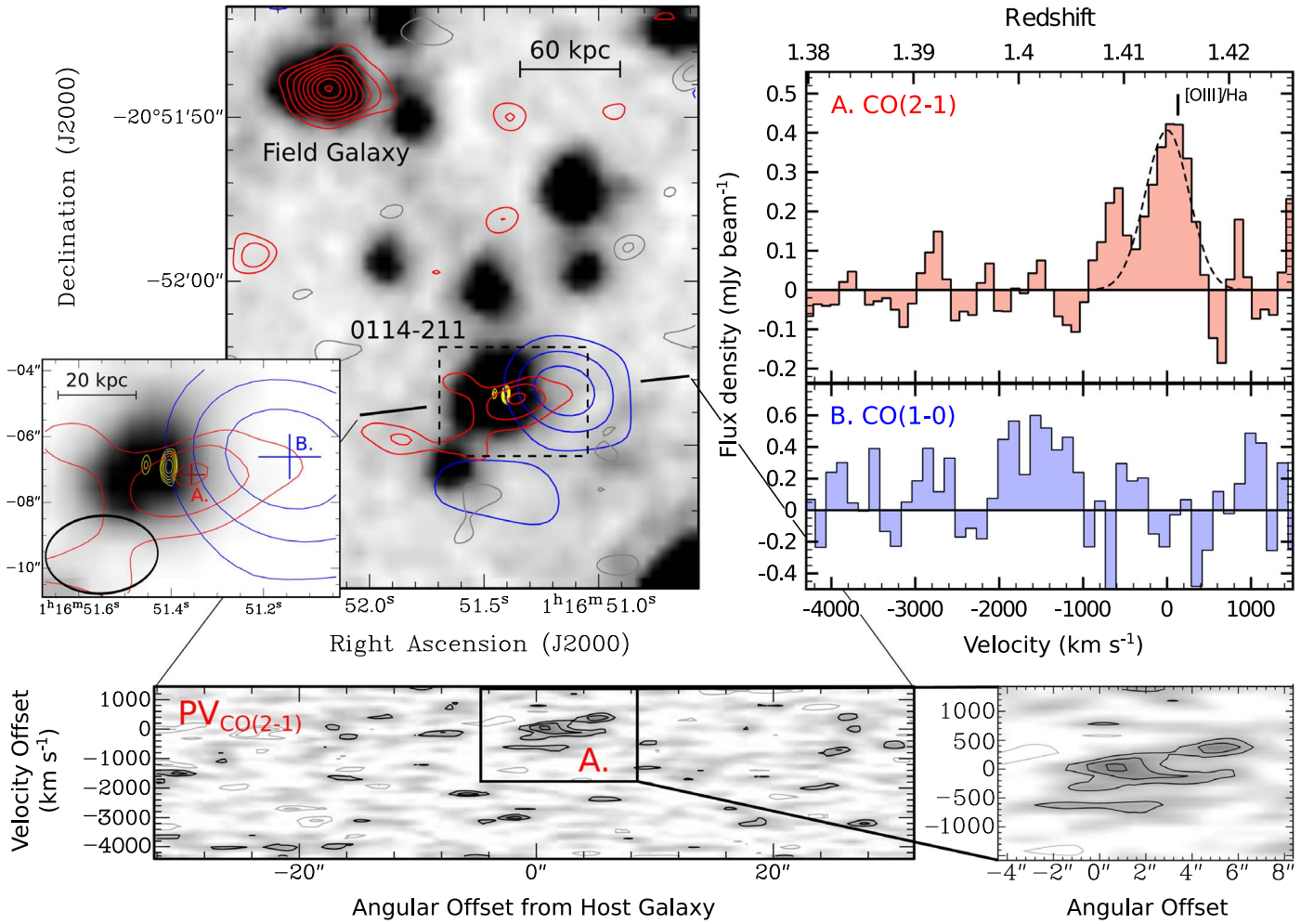

Figure 1. Molecular gas in the environment of MRC 0114-211 ($z = 1.41$). Top left: IRAC 4.5 μm image of the environment of MRC 0114-211 (Galametz et al. 2012; Wylezalek et al. 2013), with overlaid in red the contours of CO(2–1) observed with ALMA across the velocity range −773–227 km s^{-1} and in blue the contours of CO(1–0) observed with ATCA (see Paper I). CO contour levels start at 2σ and increase with 1σ, with $\sigma = 0.067$ Jy bm^{-1} × km s^{-1} for CO(2–1) and $\sigma = 0.094$ Jy bm^{-1} × km s^{-1} for CO(1–0). Negative contours are shown in gray for CO(2–1), while for clarity they are omitted for CO(1–0). The yellow contours show a Karl G. Jansky Very Large Array (VLA) 8.2 GHz image of the radio synchrotron source (De Breuck et al. 2010), with contour levels starting at 3 mJy beam^{-1} and increasing by a factor of 3. The panel in the bottom-left corner shows a zoom-in of the region around MRC 0114-211. The crosses mark the locations of the CO emission-line peaks, while their sizes indicate the astrometric uncertainties (see Table 1). The ALMA beam is indicated with the black ellipse in the bottom-left corner. Top-right: spectra of CO(2–1) (top: red) and CO(1–0) (bottom: blue) associated with MRC 0114-211. The spectra were taken at the locations of the peaks of the CO emission, which are marked with crosses in the total intensity image shown in the left zoom-in panel. The dashed line in the top plot shows a single Gaussian fit to the CO(2–1) profile, which was used to determine the redshift $z_{\rm CO(2-1)} = 1.414 \pm 0.001$. The vertical bar shows the redshift determined from [O III] and Hα (Nesvadba et al. 2017). The spectrum of CO(1–0) from Paper I was shifted in velocity to match the redshift of the CO(2–1) line. Bottom: position–velocity (PV) diagram of the ALMA CO(2–1) emission taken along a one-dimensional line in the direction that intersects the peak emission in both CO(2–1) and CO(1–0), as indicated in the top-left plot. Contour levels are at 2σ, 3σ, and 4σ, with σ the rms noise level from Table 1 (negative contours are in gray). The PV plot was not corrected for the primary beam response in order to visualize the noise level. The right panel shows a zoom-in on the CO(2–1) emission.

(VLA) data (Carilli et al. 1997) could have introduced an additional astrometric uncertainty of approximately a synthesized VLA beam.

The molecular gas masses associated with the CO(3–2) detections at the companion and the host galaxy are $M_{\rm H_2(comp)} \sim (3.9 \pm 0.5) \times 10^{10} \cdot \alpha_{\rm CO}\ M_\odot$ and $M_{\rm H_2(host)} < 3.9 \times 10^{10} \cdot \alpha_{\rm CO}\ M_\odot$, respectively (see Solomon & Vanden Bout 2005), where $\alpha_{\rm CO}$ is the CO-to-H_2 conversion factor (Bolatto et al. 2013). These estimates are based on the values of $r_{3-2/1-0}$ given in Table 2.

3. *MRC 2048-272:* The CO(1–0) emission detected with the ATCA shows a profile with two peaks, one centered around $v = 0$ km s^{-1} and the other around $v = 2500$ km s^{-1} in Figure 3. The CO(1–0) emission covers a total velocity range of ∼3500 km s^{-1}, centered on the redshift derived from Lyα (Venemans et al. 2007). The two spectral components were each detected at 3.5σ significance, resulting in a combined 5σ CO(1–0) detection of $M_{\rm H_2} \sim (6.9 \pm 1.5) \times 10^{10} \cdot \alpha_{\rm CO}\ M_\odot$ with ATCA (Paper I). The two components are cospatial and located in the CGM, at a location that is devoid of any emission in IRAC 4.5 μm imaging (Figure 3).

Our ALMA results show a CO(3–2) detection associated only with one of the two spectral components of CO(1–0), at $z_{\rm CO(3-2)} = 2.050 \pm 0.001$. The CO(3–2) signal is detected at the 4σ level. The redshift and FWHM of the CO(3–2) emission match those of the blue spectral component of CO(1–0). This blue spectral CO(1–0) component contains $M_{\rm H_2} \sim (4.5 \pm 1.1) \times 10^{10} \cdot \alpha_{\rm CO}\ M_\odot$ (Paper I).

Tables 2 and 3 further summarize the details of our ALMA results.

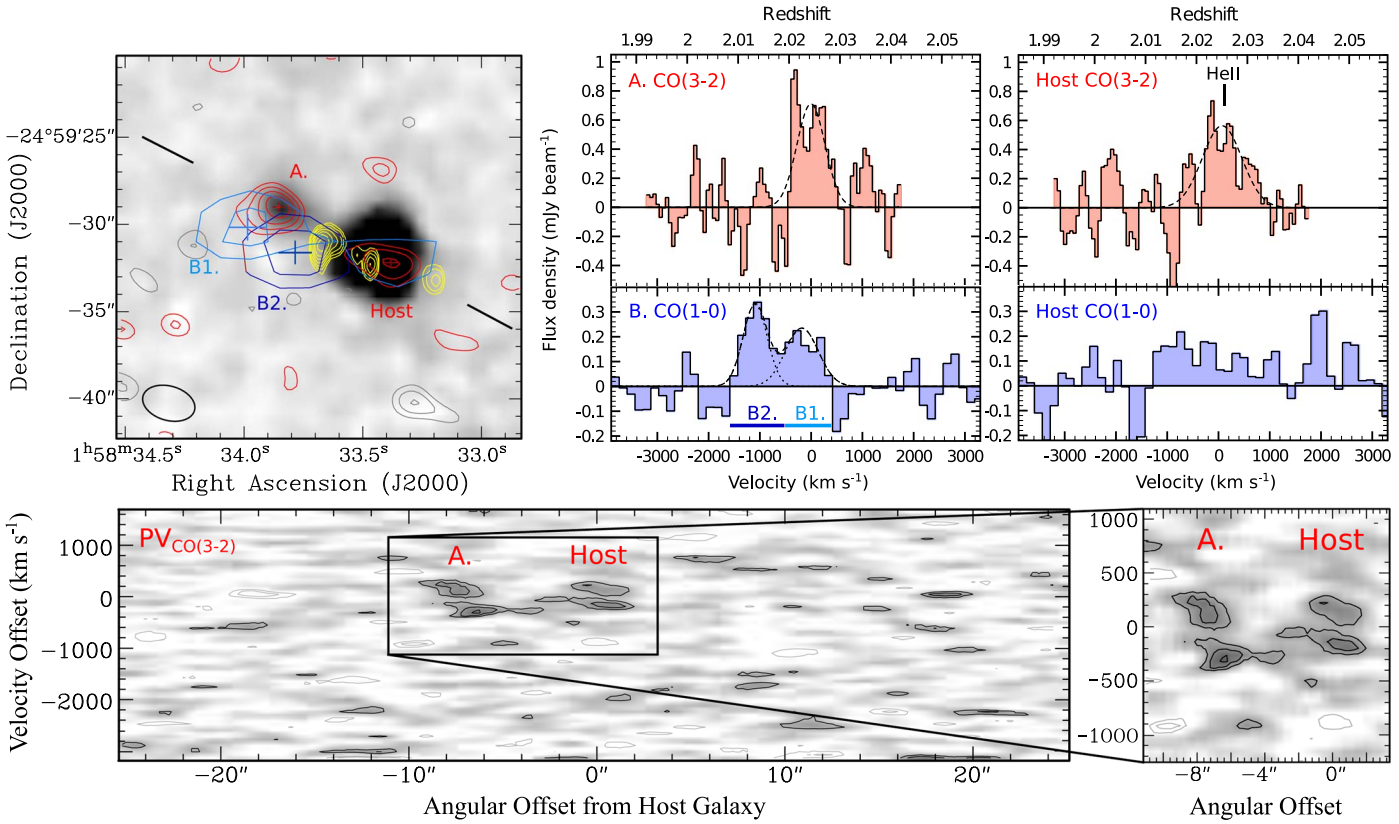

Figure 2. Molecular gas in the environment of MRC 0156-252 ($z = 2.02$). Top left: IRAC 4.5 μm image of the environment of MRC 0156-252 (Galametz et al. 2012; Wylezalek et al. 2013), with overlaid in red the contours of CO(3–2) observed with ALMA across the velocity range -417–363 km s^{-1} and in blue the contours of CO(1–0) observed with ATCA (see Paper I). The CO(1–0) emission found with ATCA is split into two components, with component B1 covering the velocity range -1583 to -508 km s^{-1} and component B2 covering -508 to 417 km s^{-1} (see Figure 7 of Paper I, corrected for the redshift of CO(3–2)). CO contour levels start at 2σ and increase with 1σ, with $\sigma = 0.080$ Jy bm^{-1} $\times$ km s^{-1} for CO(3–2), and $\sigma = 0.055$ and 0.064 Jy bm^{-1} $\times$ km s^{-1} for CO(1–0) components B1 and B2, respectively. Negative contours are shown in gray for CO(3–2), while for clarity they are omitted for CO(1–0). The crosses mark the locations of the CO emission-line peaks, while their sizes indicate the astrometric uncertainties (see Table 1). The ALMA beam is indicated with the black ellipse in the bottom-left corner. The yellow contours show a 4.7 GHz VLA image of the radio synchrotron source from Carilli et al. (1997), with contour levels starting at 0.58 mJy beam^{-1} and increasing by a factor of 2. Top right: spectra of CO(3–2) (top: red) and CO(1–0) (bottom: blue) associated with the regions "A/B" and "Host." The CO(3–2) spectrum of region "A," as well as the CO(3–2) and CO(1–0) spectra of region "Host," were taken at the locations of the peaks of the CO(3–2) emission detected with ALMA, which are marked with small red crosses in the total intensity image shown in the left panel. The CO(1–0) spectrum in region "A/B" was taken at the peak of the overall CO(1–0) emission from Paper I, taking into consideration that the ATCA beam has a large size of $6\farcs9 \times 4\farcs9$ (71°). The dashed lines show Gaussian fits to the profiles. A single Gaussian fit to the CO(3–2) profile was used to determine the redshift $z_{\rm CO(3-2)} = 2.024 \pm 0.001$. The vertical bar shows the redshift from He II derived by Galametz et al. (2013). The spectrum of CO(1–0) from Paper I was shifted in velocity to match the redshift of the CO(3–2) line. Bottom: PV diagram of the ALMA CO(3–2) emission taken along a one-dimensional line in the direction that intersects the peak emission in both region A and the core, as indicated in the top-left plot. Contour levels are at 2σ, 3σ, and 4σ, with σ the rms noise level from Table 1 (negative contours are in gray). The PV plot was not corrected for the primary beam response in order to visualize the noise level. The right panel shows a zoom-in on the CO(3–2) emission.

3.2. Results on Jet-CO Alignment

The main observational result from this paper is that the ALMA data reveal reservoirs of cold molecular gas beyond the bright radio jet in three high-z radio galaxies. This supports the previous ATCA detections of CO(1–0) in the environments, even though there are spatial and kinematics differences between the ALMA and ATCA detections.

In Figure 4 we investigate how the presence of cold molecular gas in the environment relates to the properties of the radio source. For this analysis, we do not differentiate whether the molecular gas originates from a galaxy or the CGM. Our analysis is based on large samples of previously published 4.7 and 8.2 GHz radio synchrotron data of high-z radio galaxies, which together have a median redshift of $z = 2.4$ (Carilli et al. 1997; Pentericci et al. 2000; De Breuck et al. 2010). We compare the main lobe with the fainter counter-lobe, by plotting the ratios of their flux densities and spectral indices in Figure 4. With the term "lobe" we mean the dominant hot-spot region at the resolution of the VLA data, given that only these values are available for the literature samples.

Figure 4 (left) shows the empirical result that MRC 0114-211, MRC 0156-252, and MRC 2048-262 have a bright main lobe relative to the counter-lobe, with flux-density ratios of $S_{\rm main}/S_{\rm counter} \sim 24$, 18, and 36 at 4.7 GHz, respectively. These values are high compared to other high-z radio galaxies from the literature shown in Figure 4, which show a median value of $S_{\rm main}/S_{\rm counter} \sim 2.7$. This suggests that the presence of cold molecular gas beyond the main lobe is directly related to the brightness of the synchrotron emission in these three systems.

One worry could be that the radio galaxies in Figure 4 (left) have different redshifts, and therefore the measured 4.8 and 8.2 GHz flux densities correspond to a large range in rest frequencies. We can correct for this by adjusting the observed 4.7 GHz flux densities to values expected if the sources would all be at the median redshift of $z = 2.4$ measured for the literature sample. For this, we use the spectral index α measured from the 4.8 and 8.2 GHz flux densities, where

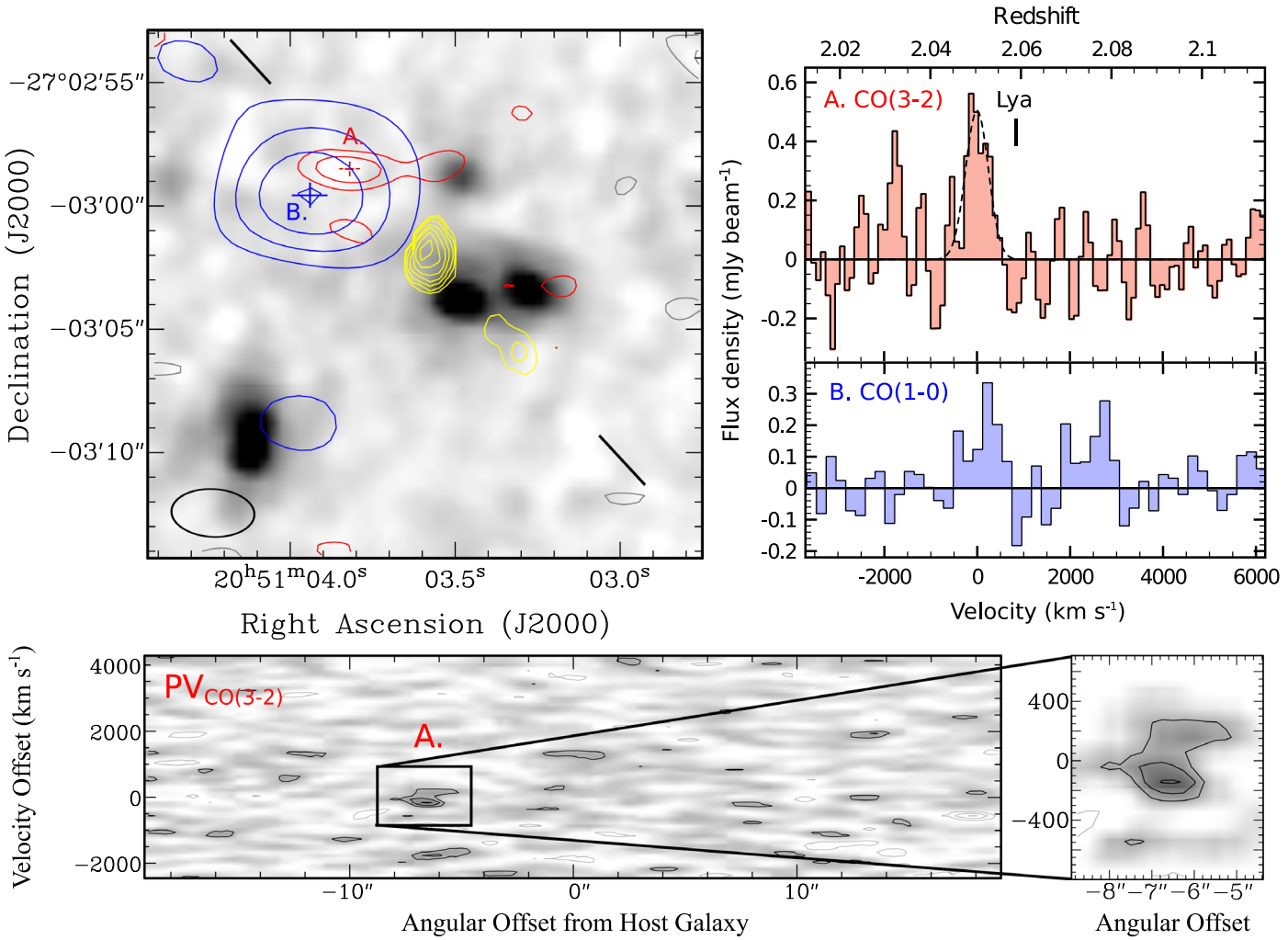

Figure 3. Molecular gas in the environment of MRC 2048-272 ($z = 2.05$). Left: IRAC 4.5 μm image of the environment of MRC 2048-272 (Galametz et al. 2012; Wylezalek et al. 2013), with overlaid in red the contours of a tentative CO(3–2) detection observed with ALMA across the velocity range −265–235 km s^{-1} and in blue the contours of CO(1–0) observed with ATCA (see Paper I). CO contour levels start at 2σ and increase with 1σ, with $\sigma = 0.056$ Jy bm^{-1} × km s^{-1} for CO(3–2) and $\sigma = 0.080$ Jy bm^{-1} × km s^{-1} for CO(1–0). Negative contours are shown in gray for CO(3–2), while for clarity they are omitted for CO(1–0). The crosses mark the location of the CO emission-line peaks, while their sizes indicate the astrometric uncertainties (see Table 1). The ALMA beam is indicated with the black ellipse in the bottom-left corner. The yellow contours show a 4.7 GHz VLA image of the radio synchrotron source from Pentericci et al. (2000), with contour levels starting at 0.5 mJy beam^{-1} and increasing by a factor of 2. Right: spectra of CO(3–2) (top: red) and CO(1–0) (bottom: blue) associated with MRC 2048-272. The spectra were taken at the locations of the peaks of the CO emission, which are marked with crosses in the total intensity image shown in the left panel. The dashed line in the top plot shows a single Gaussian fit to the CO(3–2) profile, which was used to determine the redshift $z_{\rm CO(3-2)} = 2.050 \pm 0.001$. The vertical bar shows the redshift from Lyα derived by Venemans et al. (2007). The spectrum of CO(1–0) from Paper I was shifted in velocity to match the redshift of the CO(3–2) line. Bottom: PV diagram of the ALMA CO(3–2) emission taken along a one-dimensional line along the radio axis, which also intersects the peak emission of CO(3–2). Contour levels are at 2σ, 3σ, and 4σ, with σ the rms noise level from Table 1 (negative contours are in gray). The PV plot was not corrected for the primary beam response in order to visualize the noise level. The right panel shows a zoom-in on the CO(3–2) emission.

$S_\nu = \nu^\alpha$ (with S_ν the flux density). Using α, we calculate the rest-frequency $\nu_{\rm rest} = 16$ GHz, which corresponds to $\nu_{\rm obs} = 4.7$ GHz at $z = 2.4$. As shown in Figure 4 (right), this results in an even stronger correlation.

To further investigate our results statistically, we consider that MRC 0114-211, MRC 0156-252, and MRC 2048-262 were part of a representative sample of 13 high-z radio galaxies that were studied in CO(1–0) with ATCA (Paper I). Besides MRC 0114-211, MRC 0156-252, and MRC 2048-262, only two other high-z radio galaxies from Paper I were detected in CO(1–0), namely MRC 0152-209 (a.k.a. the Dragonfly Galaxy) and MRC 1138-2623 (a.k.a. the Spiderweb Galaxy). Both the Dragonfly and Spiderweb radio galaxies also show extended CO(1–0) that stretches out to scales of 30–35 kpc distance from the host galaxy (Emonts et al. 2015a, 2015b, 2016, 2018a). Here we briefly described these two sources:

1. *MRC 0152-209 (Dragonfly Galaxy):* For the Dragonfly Galaxy, Lebowitz et al. (2023) concluded in a recent paper that the radio source brightens as it interacts with the molecular gas in the disk of a merging companion galaxy (but see also Zhong et al. 2023). This means that the Dragonfly Galaxy follows the trend seen in Figure 4, with $S_{\rm main}/S_{\rm counter}$ ∼13 at 4.7 GHz. The CO(1–0) on large scales is likely tidal debris that stretches across a total extent of ∼60 kpc (Emonts et al. 2015a).
2. *MRC 1138-262 (Spiderweb Galaxy):* The Spiderweb Galaxy (Miley et al. 2006) shows no discrepancy in the 4.7 GHz brightness ratio of the main and counter-lobe ($S_{\rm main}/S_{\rm counter} \sim 1.5$), but in this case, the large-scale

Table 2
ALMA CO Detections

MRC Source	Region	CO(J, $J-1$) Transition	$z_{CO(J,J-1)}$	FWHM $_{CO(J,J-1)}$ (km s^{-1})	$I_{CO(J,J-1)}$[a]	$L'_{CO(J,J-1)}$ (K km s^{-1} pc^2)	r $_{(J,J-1)/1-0}$[b]
0114-211 (A)[c]	ISM/CGM	$J=2$	1.414 ± 0.001	520 ± 120	0.23 ± 0.04	$(6.1 \pm 1.1) \times 10^9$	>0.34
0156-252 (A/B1)[d]	Companion	$J=3$	2.024 ± 0.001	655 ± 80	0.51 ± 0.07	$(1.2 \pm 0.2) \times 10^{10}$	0.30 ± 0.08
0156-252 (C)	Host	$J=3$	2.025 ± 0.001	910 ± 135	0.55 ± 0.09	$(1.3 \pm 0.2) \times 10^{10}$	>0.32
2048-262 (A)	CGM-1	$J=3$	2.050 ± 0.001	540 ± 95	0.29 ± 0.05	$(6.8 \pm 1.1) \times 10^9$	0.15 ± 0.04

Notes.
[a] Units for $I_{CO(J,J-1)}$ are in Jy bm^{-1} × km s^{-1}. Uncertainties include the uncertainty in the Gaussian fitting, plus an assumed 5% uncertainty in absolute flux calibration of the ALMA data.
[b] The value of $r_{J,J-1/1-0}$ is the line ratio of the CO luminosities $L'_{CO(J,J-1)}$ between the ALMA ($J=3/2$) and ATCA ($J=1$) data from Paper I. This value reflects the excitation conditions of the molecular gas.
[c] For MRC 0114-211, no CO(1–0) is detected in region A in the velocity range of the CO(2–1) detection. We assume a 3σ upper limit across the FWHM of the CO(2–1) detection.
[d] For MRC 0156-252, the CO(3–2) in region A and CO(1–0) in region B1 occur at the same redshift. Because the spatial shift between the CO peaks in these regions is less than half the FWHM of the synthesized ATCA beam, we obtained the line ratio by comparing the peak CO(3–2) emission in region A with the peak CO(1–0) emission in region B1, despite the fact that they are not exactly cospatial in Figure 2. The values for the Gaussian fitting of the CO(1–0) component of region B1 [B2] are: FWHM $_{CO(1-0)} = 755 \pm 165$ [555 ± 110] km s^{-1} and $I_{CO(1-0)} = 0.19 \pm 0.04$ [0.20 ± 0.04] mJy bm^{-1} × km s^{-1}.

CO(1–0) emission was found in all directions across the halo. Moreover, while indications for alignments between the molecular gas and the radio source are more subtle in the Spiderweb, they are present, as is evident from an increased brightness of CO(1–0) along the main jet (Emonts et al. 2016), as well as the detection of water (H_2O) emission along the jet axis (Gullberg et al. 2016). The large-scale CO(1–0) emission is likely halo gas that fuels in situ star formation across ~70 kpc in the CGM (Hatch et al. 2008; Emonts et al. 2016).

By including the Dragonfly and Spiderweb galaxies in our analysis, as well as the eight CO(1–0) nondetections from Paper I, we can perform a statistical analysis, which we will describe below. The only other high-z radio galaxy mentioned in Section 1 that has CO emission aligned with the radio source, and for which both 4.7 and 8.2 GHz observations of the radio source are available, is TXS 0828+193 (Carilli et al. 1997; Nesvadba et al. 2009; Fogasy et al. 2021). In the case of TXS 0828+193, the CO emission was detected just outside the bright hot spot of the main radio lobe (Nesvadba et al. 2009), at the location of a companion galaxy (Fogasy et al. 2021). The main lobe on the side of this gas-rich companion is a factor ~2.5 brighter than the counter-lobe (open diamond in Figure 4). However, because TXS 0828+193 was not part of the representative MRC sample that was observed with ATCA in a uniform way, we do not take it into account in our statistical analysis.

Our statistical analysis is shown in Appendix C. We base our analysis on the conservative case where we do not correct the flux-density ratio values for redshift (i.e., left panel of Figure 4). When comparing the brightness ratios of the five CO-detected radio sources from Paper I (which all show large-scale CO emission) with those of the much larger literature sample of high-z radio galaxies, a Kolmogorov–Smirnov (K-S) test reveals that the probability that both samples are drawn from the same distribution is only ~0.5% (see Appendix C for details). Therefore, the correlation in Figure 4 between the presence of circumgalactic molecular gas beyond the radio source and an increased brightness ratio between main lobe and counter-lobe, is statistically inconsistent with random sampling.

The correlation shown in Figure 4 indicates that the increased brightness in the radio flux density of the main lobe is a direct result of the presence of cold molecular gas at or near the location of the radio hot spot. The lobe brightening cannot be explained by Doppler boosting, which is the effect where the approaching radio jet increases its apparent brightness due to relativistic effects, because this only depends on the inclination angle of the jet and not on environmental conditions. Moreover, the 4.7 and 8.2 GHz measurements of the "lobe" predominantly reflect the hot-spot regions (Section 3.2), which are the working surface where the lobe interacts with the CGM at subrelativistic speeds. Although some Doppler boosting likely still occurs for the main hot-spot region, this typically results in a brightening of the flux density by a factor of at most a few (Komissarov & Falle 1996), i.e., less than what we observe for MRC 0114-211, MRC 0156-252, MRC 2048-272, and also MRC 0152-209 (Dragonfly Galaxy; Lebowitz et al. 2023).

There is also a tentative indication from Figure 4 that the 4.7–8.2 GHz spectral index is less steep within the bright main lobe among the three high-z radio galaxies that we study in this paper. However, based on the same K-S test as for the flux-density ratios, the difference in spectral-index values between the radio galaxies with detections of circumgalactic molecular gas and the large sample of high-z radio galaxies is not statistically significant.

In summary, our results suggest that in the presence of molecular gas beyond the radio source, the radio synchrotron emission brightens. We will further discuss this result in Section 4.

4. Discussion

The alignments that we observe between the radio sources and molecular gas reservoirs, as well as the increased flux density of the main lobe compared to the counter-lobe in the presence of these gas reservoirs, strongly suggest that jet–cloud interactions take place in the circumgalactic environment of our ALMA targets, even at distances out to ~50 kpc from the radio host galaxy. Eales (1992) suggested that such alignments can be explained by radio sources expanding into asymmetric gas distributions, and experiencing an increase in synchrotron luminosity that is, on average, largest in the direction where the gas density is highest. In addition, West (1994) showed that

Table 3
ALMA CO Nondetections in CGM (after Smoothing)

Source MRC	Region	rms (Smoothed) (mJy bm^{-1} chan$_{100}^{-1}$)	$I_{CO(J,J-1)}$ [a] (Jy bm^{-1} × km s^{-1})	$I_{CO(1-0)}$ [b] (Jy bm^{-1} × km s^{-1})	r $_{(J,J-1)/1-0}$
0114-211 (B)	CGM	0.32	<0.23	0.43 ± 0.08	<0.13
0156-252 (B2)	ISM/CGM	0.55	<0.39	0.20 ± 0.04	<0.22
2048-262 (B)	CGM-2	0.35	<0.26	0.19 ± 0.05	<0.16

Notes. *rms noise level per 100 km s^{-1} channel, after tapering and smoothing the ALMA data to the same resolution as the ATCA CO(1–0) data from Paper I.
[a] For the ALMA nondetections in the CGM, we use conservative limits based on the tapered/smoothed ALMA data and assuming a 3σ limit over the FWHM of the CO(1–0) emission.
[b] See Paper I and caption of Table 2 for details on the CO(1–0) detections, with the assumption of FWHM = 0.5 × FWZI.

radio sources tend to align with the major axis of the mass distribution on large scales. Therefore, these earlier theories agree with our observations. In this Section, we will explore the cause and effect that may lead to our observed alignments and lobe brightening.

4.1. Jet–Cloud Interactions: Synchrotron Brightening

The brightening of the radio lobe in the presence of cold molecular gas suggests that the radio lobe is confined as it propagates into the molecular gas reservoir. As energy and momentum are being exchanged between the gas and the lobes, the gas experiences an increased velocity dispersion (e.g., Mandal et al. 2021; Meenakshi et al. 2022). The fact that the CO(1–0) profiles of MRC 0114-211, MRC 0156-252, and MRC 2048-262 are fairly broad, with a full width at zero intensity (FWZI) ranging from 1100–3600 km s^{-1}, agrees with this and suggests that the molecular gas is turbulent. It is likely that compression and possible tangling of the magnetic fields, combined with the increased density of particles, boosts the radio synchrotron luminosity (e.g., Gopal-Krishna 1991; Morganti et al. 2011), although Anderson et al. (2022) showed that jet–gas interactions also occur along radio sources with well-ordered, coherent magnetic fields that magnetize their surrounding environment. Among our sample, there is also a tentative indication that the spectral index of the main lobe becomes less steep compared to the counter-lobe. If confirmed, this may indicate that shocks re-accelerate electrons in the main lobe, or that particle replenishment is still ongoing and therefore synchrotron losses due to spectral aging are less severe in the lobe that is confined by interaction with the molecular gas (e.g., Blundell & Rawlings 2000).

The bulk of the molecular gas reservoirs, as identified by the peak of the CO emission, appear to be located well beyond the radio hot spot. For MRC 0156-252 and MRC 2048-272, the distance between the hot spot and the peak of the ALMA detected CO(3–2) emission appears to be ∼25 and ∼40 kpc, respectively. However, even though the working surface of the radio jet is thought to be the brightest where it encounters the densest medium (e.g., Barthel & Arnaud 1996), the molecular gas reservoirs likely cover a large (tens of kiloparsecs) scale, and the interaction between the radio source and the molecular gas occurs at the boundary of the gas reservoir. The gas density even at the edge of the molecular reservoirs is likely high enough for this, considering that jet–gas interactions are frequently observed to be associated with much less dense gas, such as warm gas traced in Lyα, Hα, and [O III] (e.g., Villar-Martín et al. 2003; Humphrey et al. 2006; Nesvadba et al. 2017).

Under this scenario that jet–cloud interactions brighten the radio synchrotron emission, our observed alignments between radio sources and CO-emitting gas reservoirs could in part be due to intrinsically fainter radio sources being pushed into the flux-selected samples of high-z radio galaxies (see also Eales 1992). This scenario was also suggested in the recent study of the Dragonfly Galaxy (MRC 0152-209) by Lebowitz et al. (2023). The scenario where jet–cloud interactions convert jet power into radio luminosity also agrees with studies of mostly ionized and neutral gas around low-z radio sources (e.g., van Breugel et al. 1985; Fosbury et al. 1998; Villar-Martín et al. 1999, 2017; Tadhunter et al. 2000; Morganti et al. 2002, 2011; Murthy et al. 2020) and has been proposed to explain the relatively large fraction of young and compact radio sources seen among starbursting radio galaxies at low-z (Tadhunter et al. 2011).

4.1.1. Jet-induced Enrichment and Cooling?

Figure 4 would be more difficult to explain if the molecular gas reservoirs would be merely a manifestation of the effects of the radio source, such as jet-induced enrichment and cooling, because this would likely be related to the *total* radio power rather than the flux-density ratio of the lobe and counter-lobe. Nevertheless, in general, the most robust detections of large-scale (tens of kiloparsecs to 100 kpc) molecular gas in circumgalactic environments are predominantly found to be associated with radio galaxies and radio-loud quasi-stellar objects (QSOs), while radio-quiet QSOs show less extended molecular gas reservoirs (Jones et al. 2023; Li et al. 2023). Therefore, it is worth exploring the effect that the radio jets may have on surrounding gas reservoirs. Radio-loud active galactic nucleus (AGN) activity is a recurrent phenomenon, so previous jet activity may also have contributed to creating the CO-emitting reservoirs.

Paper I described in detail that the effect of the radio jet on the circumgalactic medium may include chemical enrichment and gas cooling (see also Klamer et al. 2004). For nearby brightest clusters galaxies, Kirkpatrick et al. (2009) and Kirkpatrick et al. (2011) found that the radio source can drive chemical enrichment along the radio axis, typically over multiple episodes of radio-source activity. At high redshifts, such enrichment processes likely contribute to the near-solar metallicities observed across extended emission-line regions of high-z radio galaxies and quasars (e.g., Vernet et al. 2001; Humphrey et al. 2008; Prochaska & Hennawi 2009). These processes could deposit the carbon and oxygen elements needed to form the large reservoirs of CO-emitting gas.

In addition, the propagating radio jet likely compresses and cools the enriched CGM through shocks (e.g., Mellema et al.

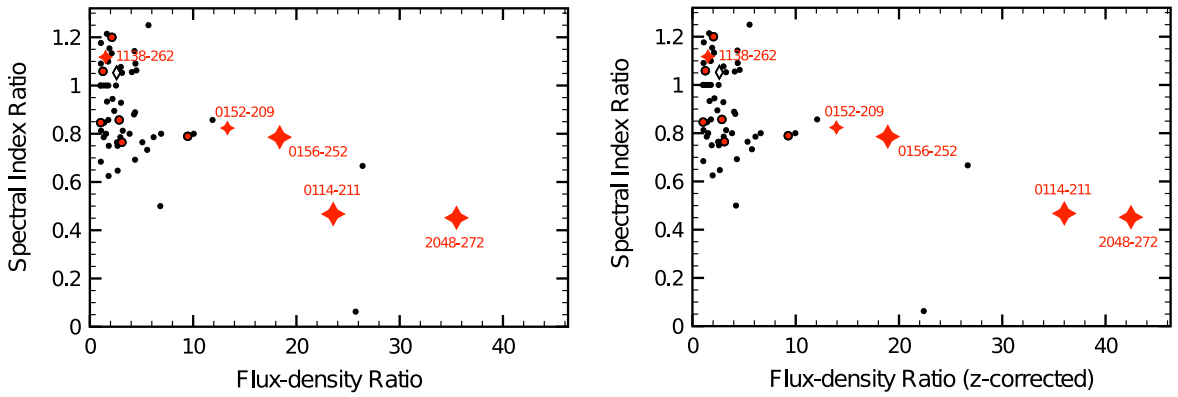

Figure 4. Left: plot showing on the horizontal axis the measured 4.7 GHz flux-density ratio between the lobe and counter-lobe of high-z radio galaxies. The vertical axis shows the corresponding ratio of the 4.7–8.2 GHz spectral index of main and counter-lobe. Higher lobe ratios indicate a larger difference in flux density between the main lobe and counter-lobe, while progressively lower spectral-index ratios indicate that the brighter main lobe has a progressively shallower radio spectral index compared to the counter-lobe. Red symbols show high-z radio galaxies studied in CO(1–0) with ATCA (Paper I), with red stars showing the five CO(1–0) detections, and small red dots showing the CO(1–0) nondetections. The large red stars are the three sources discussed in Section 3.1 of this paper. The black dots are high-z radio galaxies from the literature, acquired from Carilli et al. (1997), Pentericci et al. (2000), and De Breuck et al. (2010). Measurements from the continuum imaging by De Breuck et al. (2010) are summarized in Appendix B. The black open diamond is TXS 0828+193 (Section 3.2). Right: same as left panel, but the flux densities and corresponding flux-density ratios are corrected for redshift, using the spectral index, to reflect a rest-frequency of $\nu_{\rm rest} = 16.0$ GHz, which corresponds to $\nu_{\rm obs} = 4.7$ GHz for a source at the median redshift of $z = 2.4$ measured for the full literature sample. The spectral indices are not affected by this z-correction.

2002; Sutherland et al. 2003; Fragile et al. 2004; Gaibler et al. 2012; Fragile et al. 2017; Mandal et al. 2021). This process was suggested to occur in the Spiderweb radio galaxy (MRC 1138-262), where both enhancements in CO(1–0) and H_2O emission were found along the radio jet, likely as a result of gas cooling behind slow shocks that propagate through the dense, multiphase gas (Gullberg et al. 2016; Emonts et al. 2016). Such gas cooling may result in jet-triggered star formation; see, for example, the case of Minkowski's Object (Croft et al. 2006; Salomé et al. 2015), 4C 41.17 (Dey et al. 1997; Nesvadba et al. 2020), and possible other high-z radio galaxies (Klamer et al. 2004). This could explain alignments found between high-z radio jets and large-scale UV rest-frame continuum and submillimeter emission (Chambers et al. 1987; McCarthy et al. 1987b; Begelman & Cioffi 1989; De Young 1989; Rees 1989; Bicknell et al. 2000; Stevens et al. 2003; Ivison et al. 2012), or the enhanced rates of star formation associated with radio-loud AGNs (Zinn et al. 2013).

In summary, while our CO results are in agreement with literature work indicating that radio sources may enrich or cool gas in their environment, our work (Figure 4) predominantly shows that the cold gas directly affects the radio source, enhancing its brightness due to jet–cloud interactions.

4.2. Gas Excitation: Interstellar Medium or Circumgalactic Medium?

A detailed analysis of the physical properties of the molecular gas in the circumgalactic environment of MRC 0114-211, MRC 0156-252, and MRC 2048-262 is difficult, given the low signal-to-noise ratio (S/N) and limited resolution of our ALMA and ATCA detections. Nevertheless, we here provide a first-order analysis of the properties of the molecular gas reservoirs, to obtain some insight into their nature.

For MRC 0114-211, the ALMA detection of CO(2–1) (region A) peaks at roughly 10 kpc from the center of the radio galaxy and very close to the radio hot spot. For MRC 0156-252, the ALMA detection (region A) coincides with a detection in the IRAC Band 2 image, and is thus likely associated with a companion galaxy. For both cases, the line ratios of $r_{2-1/1-0} > 0.34$ and $r_{3-2/1-0} \sim 0.30$ (Table 2) are consistent with excitation conditions found in the ISM of high-z galaxies (e.g., Dannerbauer et al. 2009; Ivison et al. 2011; Bothwell et al. 2013; Aravena et al. 2014; Daddi et al. 2015). On the other hand, the line ratios are significantly lower for the CO(1–0) detections farther out from the host or any companion galaxy, with $r_{2-1/1-0} < 0.13$ for region B in MRC 0114-211, $r_{3-2/1-0} < 0.22$ for region B2 in MRC 0156-252, and $r_{3-2/1-0} \lesssim 0.16$ in MRC 2048-262 (Table 3). Despite the uncertainty associated with this analysis, our results suggests that while part of the CO emission in MRC 0114-211 and MRC 0156-252 is likely associated with the ISM of either the host or a companion galaxy, at least some fraction of the CO(1–0) emission in these two systems, and possibly all of the CO emission in the third system MRC 2048-272, appears to be part of the CGM. This molecular gas in the CGM has a low excitation, but it is not clear from our data whether it is diffuse or clumpy.

For future work, our results on the gas excitation strongly suggest that observations of the CO ground-transition that are sensitive to detecting low-surface-brightness emission are critical for recovering widespread cold molecular gas reservoirs. ALMA Band 1 will soon allow observations of CO(1–0) out to redshifts of $z \lesssim 2.3$ ($\nu_{\rm obs} \geqslant 35$ GHz). In terms of surface-brightness sensitivity, ALMA's extremely compact array configurations are an improvement over the VLA in D-configuration, whose Ka- and Q-band receivers operate in the same frequency regime. On longer timescales, the next-generation VLA (ngVLA) will be able to target CO(1–0) at almost any redshift (Decarli et al. 2018; Murphy 2018). In particular when optimized for surface-brightness sensitivity with a densely packed configuration of antennas in the central kilometer-scale region (Carilli et al. 2021), the core of the ngVLA will be a critical complement to ALMA for tracing low-J CO in the CGM at the highest redshifts (Emonts et al. 2018b). Complementary ALMA observations of the high-J CO

transitions at higher frequencies can easily over-resolve or resolve out emission from widespread gas reservoirs. A large millimeter single-dish telescope, such as the Atacama Large Aperture Submillimeter Telescope (Bertoldi 2018; Cicone et al. 2019; Klaassen et al. 2020), can recover all of the flux of the high-J CO lines.

5. Conclusions

We presented the detection of CO(2–1) or CO(3–2) emission in the environments of three high-z radio galaxies, MRC 0114-211 ($z = 1.41$), MRC 0156-252 ($z = 2.02$), and MRC 2048-272 ($z = 2.05$). Our ALMA data support previous results from a CO(1–0) survey performed with ATCA, which detected CO(1–0) emission from cold molecular gas in the halo environments of these sources. We derive the following conclusions:

1. The CO is found along the radio axis but beyond the main radio lobe. This confirms that the "alignment effect", which is often observed for different constituents of high-z radio galaxies, also applies to cold molecular gas on large scales in these sources.
2. For MRC 0114-211 and MRC 0156-252, part of the observed molecular gas is likely ISM from the host or a companion galaxy, respectively. However, in other parts of the molecular reservoirs of these two sources, as well as for the case of MRC 2048-272, the CO(2–1) or CO(3–2) emission does not appear to be associated with any galaxy and is faint compared to CO(1–0), with $r_{3-2/1-0}$ and $r_{2-1/1-0}$ values $\lesssim$0.2. This suggests that we may also be tracing molecular gas with low excitation in the CGM.
3. The presence of cold molecular gas in the environment of our sources (whether from the ISM or CGM) correlates with an increase in the brightness of the main radio lobe. This is derived from high ratios in the 4.7 GHz flux density of the main lobe compared to the counter-lobe, with $S_{\rm main}/S_{\rm counter} \sim 18$–$36$ for our three sources, compared to a median value of $S_{\rm main}/S_{\rm counter} \sim 2.7$ for a large sample of high-z radio galaxies from the literature. Based on a K-S test, we show that, at a statistical significance of 99.5%, there is a difference in this ratio of the lobe brightness between high-z radio galaxies with CO detected in the environment and the larger population of high-z radio galaxies. This suggests that the cold gas affects the properties of the radio source, and that the alignment effect may in part be caused by intrinsically fainter radio sources, the brightness of which is enhanced enough to enter the flux-selected samples of high-z radio galaxies (see also Lebowitz et al. 2023). The radio source may also affect the molecular gas reservoir though enrichment and cooling, but this is more speculative from our data.

Our work confirms the importance of studying the interplay between radio sources and cold gas in the circumgalactic environments of high-z galaxies. To understand how these results compare to the general population of galaxies in the early universe, future millimeter observations with compact interferometric arrays that are sensitive to recovering low-surface-brightness emission of low-J CO are critical for studying the total budget of cold gas across the universe.

Acknowledgments

We thank Donald Terndrup for useful discussions during the preparation of this paper. We also thank the referee for valuable feedback. This paper makes use of the following ALMA data: ADS/JAO.ALMA#2015.1.00897.S. ALMA is a partnership of ESO (representing its member states), NSF (USA) and NINS (Japan), together with NRC (Canada), MOST and ASIAA (Taiwan), and KASI (Republic of Korea), in cooperation with the Republic of Chile. The Joint ALMA Observatory is operated by ESO, AUI/NRAO, and NAOJ. The National Radio Astronomy Observatory is a facility of the National Science Foundation operated under cooperative agreement by Associated Universities, Inc. The Australia Telescope Compact Array is part of the Australia Telescope National Facility (https://ror.org/05qajvd42), which is funded by the Australian Government for operation as a National Facility managed by CSIRO. Based on observations with the NASA/ESA Hubble Space Telescope obtained from the Data Archive at the Space Telescope Science Institute, which is operated by the Association of Universities for Research in Astronomy, Incorporated, under NASA contract NAS5-26555. Support for program numbers HST-AR-16123.001-A and HST-GO-16891.002-A was provided through a grant from the STScI under National Aeronautics and Space Administration (NASA) contract NAS5-26555. M.V.M. acknowledges support from grant PID2021-124665NB-I00 by the Spanish Ministry of Science and Innovation (MCIN) / State Agency of Research (AEI)/10.13039/501100011033 and by the European Regional Development Fund (ERDF) "A way of making Europe."

Facilities: ALMA, ATCA, VLA, Spitzer, HST.

Software: CASA (CASA Team et al. 2022).

Appendix A
CO-bright Galaxy in the Field of MRC 0114-211

A bright line emitter was found in the field of MRC 0114-211 at R.A. = $01^{\rm h}16^{\rm m}52\overset{\rm s}{.}17$, decl = $-20°\,51'\,48\overset{''}{.}2$, which is a distance of $\sim$20″ ($\sim$170 kpc) northeast of the radio galaxy. The line emitter is detected in both CO(2–1) and CO(1–0), and has the same redshift as MRC 0114-211 ($z = 1.414$). This galaxy has a counterpart in the IRAC 4.5 μm image of Figure 1.

The integrated CO(2–1) emission of this field galaxy is the strongest signal found among the ALMA data sets used in this paper, and is detected at an integrated S/N level of S/N $\approx$10. This means that the CO(2–1) emission in the ALMA data is bright enough to attempt a meaningful deconvolution and restoration ("cleaning") of the signal. We cleaned the signal in a circular aperture with a radius of 2″ centered on the peak of the CO(2–1) emission, down to a threshold of 2.5σ in each channel. When processing and imaging the cleaned data in the same way as the data described in Section 2, the CO(2–1) peak flux-density of this field galaxy decreased by only 1.6% compared to the case of no deconvolution, while the peak flux-density of the CO(2–1) emission around MRC 0114-211 decreased by only 2.4%. These values are lower than the assumed 5% uncertainty in absolute flux calibration. Also, no significant difference in the morphology of the signal is seen down to the 2σ level shown in Figure 1 when taking the same channel ranges for the integrated emission. Therefore, deconvolution does not affect the results presented in this paper, and at the low clean threshold that we had to adopt could include components that are dominated by noise. We therefore

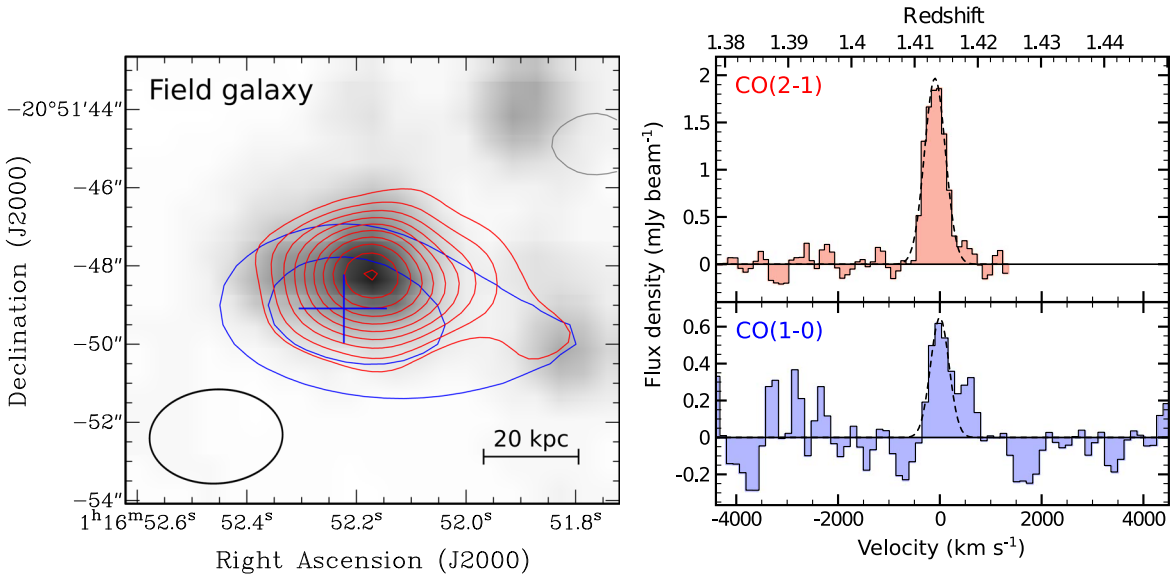

Figure 5. Molecular gas in the CO-bright field galaxy northeast of MRC 0114-211 ($z = 1.41$). Left: IRAC 4.5 μm image of the field galaxy (Galametz et al. 2012; Wylezalek et al. 2013), with overlaid in red the contours of CO(2–1) observed with ALMA across the velocity range −468–332 km s^{-1}, and in blue contours of CO(1–0) observed with ATCA. CO contour levels start at 2σ and increase with 1σ, with $\sigma = 0.085$ Jy bm^{-1} × km s^{-1} for CO(2–1) and $\sigma = 0.082$ Jy bm^{-1} × km s^{-1} for CO(1–0), after correcting for the primary beam response. Negative contours are shown in gray for CO(2–1), while for clarity they are omitted for CO(1–0). The blue cross marks the location of the CO(1–0) emission-line peak, while its size indicates the astrometric uncertainty. The astrometric uncertainty for the ALMA signal of CO(2–1) is not significant compared to CO(1–0) (see Table 1). The ALMA beam is indicated with the black ellipse in the bottom-left corner. Right: spectra of CO(2–1) (top: red) and CO(1–0) (bottom: blue) associated with the field galaxy. The spectra were taken at the locations of the peaks of the CO emission, which for CO(1–0) is marked with a cross in the total intensity image shown in the left panel. Flux densities were corrected for the primary beam response. The dashed lines show single Gaussian fits to the CO profiles. The central velocity $v = 0$ km s^{-1} is the same as in Figure 1, namely the redshift of MRC 0114-211 derived from the CO(2–1) emission in region "A."

use the cleaned data cube only for the analysis of the field galaxy in this Appendix.

Figure 5 shows the CO(2–1) and CO(1–0) detection of this field galaxy. The data properties are the same as in Table 1, with the only difference being that we applied a primary beam correction to recover accurate flux values this far from the center of the image. To derive CO intensities, we fit a Gaussian model to the CO lines. The resulting line properties for the ALMA CO(2–1) data [ATCA (CO(1–0)) data] are $v_{\rm CO} = -100 \pm 10$ [0 ± 60] km s^{-1}; FWHM$_{\rm CO}$ = 480 ± 30 [430 ± 130] km s^{-1}; and $I_{\rm CO} = 1.01 \pm 0.08$ [0.30 ± 0.08] mJy bm^{-1} km s^{-1}. The total H_2 mass of the field galaxy derived from CO(1–0) is $M_{\rm H_2} = (3.0 \pm 0.8) \times 10^{10} \cdot \alpha_{\rm CO}\ M_\odot$ (Solomon & Vanden Bout 2005), and the ratio of the CO luminosities is $r_{2-1/1-0} = 0.84 \pm 0.23$. This is consistent with values found for other high-z galaxies (e.g., Dannerbauer et al. 2009; Ivison et al. 2011; Bothwell et al. 2013; Aravena et al. 2014; Daddi et al. 2015). There is a tentative indication that the CO emission may be extended toward the west, but this needs to be confirmed.

Appendix B
Radio Continuum Properties of Three ATCA Sources

In this Appendix, we provide the continuum properties of three sources that are part of our ATCA sample, MRC 0114-211, MRC 0324-228, and MRC 0350-279; all three were imaged at 4.7 GHz and 8.2 GHz by De Breuck et al. (2010). The flux densities and spectral indices are measured from the continuum images of De Breuck et al. (2010), and the results are summarized in Table 4.

Table 4
Continuum Properties of Three ATCA Sources

Source	Brightest Hot Spot		Faintest Hot Spot	
	$I_{4.7\ \rm GHz}$ [†]	$\alpha_{4.7}^{8.2}$	$I_{4.7\ \rm GHz}$ [†]	$\alpha_{4.7}^{8.2}$
MRC 0114-211	1.06	−1.1	0.045	−2.3
MRC 0324-228	0.041	−1.8	0.019	−1.5
MRC 0350-279	0.033	−1.8	0.026	−1.7

Note. Units for $I_{4.7\ \rm GHz}$ are in Jy beam^{-1}.

Appendix C
Statistical Analysis

In this Appendix, we investigate whether there is a statistical significance to the observed correlation that the high-z radio sources with extended CO emission also have a relatively bright main lobe compared to the counter-lobe (Figure 4, left). For this, we use a one-tailed K-S test for two samples of unequal size. The first sample is our ATCA sample from Paper I. Out of the 13 MRC sources observed by ATCA, only 11 have information regarding their radio continuum properties available in Carilli et al. (1997), Pentericci et al. (2000), or De Breuck et al. (2010). We divide these 11 MRC sources into a subsample of five detections and a subsample of six nondetections in CO(1–0). The nondetections from the ATCA sample have a 3σ upper limit of $L'_{\rm CO(1-0)}$ that is equal to or smaller than $L'_{\rm CO(1-0)}$ of the five ATCA detections (Paper I). Therefore, we do not expect a bias regarding the CO(1–0) sensitivity across the sample observed with ATCA. The second sample is the literature sample of high-z radio galaxies shown in Figure 4, but excluding the MRC sources that we observed with ATCA. Figure 6 shows the results from our K-S analysis.

Panel (A) of Figure 6 shows that when comparing the literature sample with the full ATCA sample (detections and nondetections), the probability that both samples are drawn from the same distribution is just above 10%. This means that there is no statistical difference between the two samples, which in turn means that there were no significant biases that influenced the selection of the ATCA sample in terms of the lobe-ratio values shown in Figure 4. Panel (B) shows that the same conclusion can be drawn when considering just the nondetections in the ATCA sample (red dots in Figure 4), with an even better correspondence with the literature sample. However, panel (C) shows that when considering only the CO detections in the ATCA sample (stars in Figure 4, left), the probability that this sample of five sources is drawn from the same distribution as the literature sample is only 0.5%. This means that there is a statistical difference in the ratio of the lobe brightness between our sample of radio galaxies with CO detected in the environment and the larger population of high-z radio galaxies. We note that this result is obtained by including MRC 1138-262, which shows extended CO(1–0) emission in all directions across the halo (Emonts et al. 2016). If we would only consider the four ATCA sources of interest for this paper, namely those sources with extended CO detected along the radio axis, then this would even further decrease the probability that their high ratio in lobe brightness is the result of random sampling.

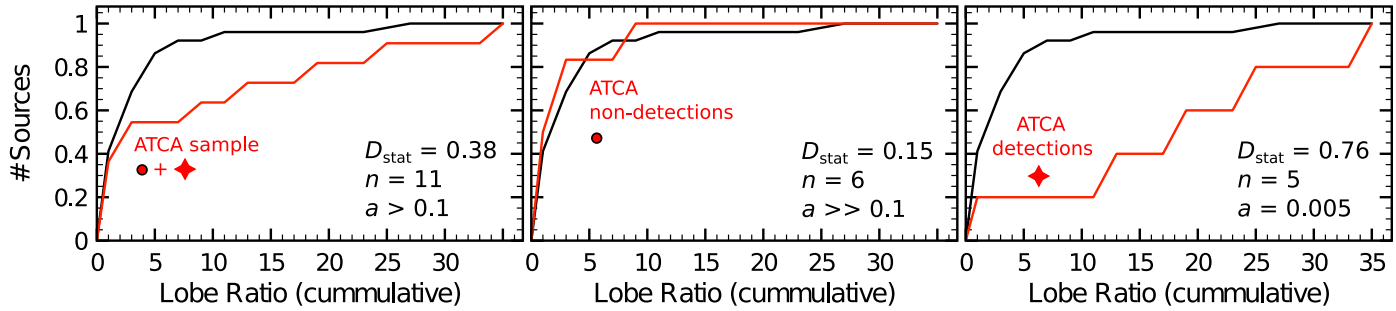

Figure 6. Statistical analysis on the significance of high lobe-ratio values among the high-z radio galaxies with extended CO emission, using a one-tailed K-S test for two samples of unequal size. Left (A): cumulative distribution of the 4.7 GHz lobe ratios for the full ATCA CO(1–0) sample of 11 sources (detections and nondetections) from Figure 4 (red line), compared to the other 51 high-z radio galaxies from the literature shown in Figure 4 that were not targeted with ATCA (black line). Middle (B): same as left panel, but only including the six ATCA CO(1–0) nondetections (red line). Right (C): same as left panel, but only including the five ATCA CO(1–0) detections. In the legend, $D_{\rm stat}$ is the K-S test statistic, n is the number of sources in the ATCA sample that are included in the analysis, and a is the probability that the two samples are drawn from the same probability distribution. Only the sample of the ATCA CO detections (panel (C)) shows a statistically significant difference in lobe ratio with the literature sample of high-z radio galaxies.

ORCID iDs

Bjorn H. C. Emonts https://orcid.org/0000-0003-2983-815X
Matthew D. Lehnert https://orcid.org/0000-0003-1939-5885
Carlos De Breuck https://orcid.org/0000-0002-6637-3315
Chris Carilli https://orcid.org/0000-0001-6647-3861

References

Anderson, C. S., Carilli, C. L., Tozzi, P., et al. 2022, ApJ, 937, 45
Aravena, M., Hodge, J. A., Wagg, J., et al. 2014, MNRAS, 442, 558
Aravena, M., Wagg, J., Papadopoulos, P. P., & Feain, I. J. 2011, ApJ, 737, 64
Barthel, P., Haas, M., Leipski, C., et al. 2012, ApJL, 757, L26
Barthel, P. D., & Arnaud, K. A. 1996, MNRAS, 283, L45
Barthel, P. D., Vestergaard, M., & Lonsdale, C. J. 2000, A&A, 354, 7
Begelman, M. C., & Cioffi, D. F. 1989, ApJL, 345, L21
Bertoldi, F. 2018, Atacama Large-Aperture Submm/mm Telescope (AtLAST), Zenodo, doi:10.5281/zenodo.1158842
Bicknell, G. V., Sutherland, R. S., van Breugel, W. J. M., et al. 2000, ApJ, 540, 678
Blandford, R. D. 2001, PThPS, 143, 182
Blundell, K. M., & Rawlings, S. 2000, AJ, 119, 1111
Bolatto, A. D., Wolfire, M., & Leroy, A. K. 2013, ARA&A, 51, 207
Bothwell, M. S., Smail, I., Chapman, S. C., et al. 2013, MNRAS, 429, 3047
Broderick, J. W., Drouart, G., Seymour, N., et al. 2022, PASA, 39, e061
Carilli, C. L., Mason, B., Rosero, V., et al. 2021, Configuration: Reference Design Rev D DescriptionMemo No. 92, Next Generation VLA
Carilli, C. L., Röttgering, H. J. A., van Ojik, R., Miley, G. K., & van Breugel, W. J. M. 1997, ApJS, 109, 1
Carson, J. E., Larkin, J. E., McLean, I. S., et al. 2001, ApJ, 563, 63
CASA Team, Bean, B., Bhatnagar, S., et al. 2022, PASP, 134, 114501
Chambers, K. C., Miley, G. K., & van Breugel, W. 1987, Natur, 329, 604
Chambers, K. C., Miley, G. K., & van Breugel, W. J. M. 1990, ApJ, 363, 21
Chambers, K. C., Miley, G. K., van Breugel, W. J. M., et al. 1996a, ApJS, 106, 215
Chambers, K. C., Miley, G. K., van Breugel, W. J. M., et al. 1996b, ApJS, 106, 247
Cicone, C., De Breuck, C., Chen, C.-C., et al. 2019, BAAS, 51, 82
Claude, S., Dindo, P., Erickson, D., et al. 2005, in IRMMW-THz 2005, ed. K. J. Button, G. R. Neil, & B. Danly (Piscataway, NJ: IEEE), 407
Croft, S., van Breugel, W., de Vries, W., et al. 2006, ApJ, 647, 1040
Daddi, E., Bournaud, F., Walter, F., et al. 2010, ApJ, 713, 686
Daddi, E., Dannerbauer, H., Liu, D., et al. 2015, A&A, 577, A46
Dannerbauer, H., Daddi, E., Riechers, D. A., et al. 2009, ApJL, 698, L178
Dannerbauer, H., Kurk, J. D., De Breuck, C., et al. 2014, A&A, 570, A55
De Breuck, C., Lundgren, A., Emonts, B., et al. 2022, A&A, 658, L2
De Breuck, C., Seymour, N., Stern, D., et al. 2010, ApJ, 725, 36
De Breuck, C., van Breugel, W., Röttgering, H., et al. 2001, AJ, 121, 1241
De Breuck, C., van Breugel, W., Röttgering, H. J. A., et al. 2000, A&AS, 143, 303
De Young, D. S. 1989, ApJL, 342, L59
Decarli, R., Carilli, C., Casey, C., et al. 2018, in ASP Conf. Ser. 517, Science with a Next Generation Very Large Array, ed. E. Murphy (San Francisco, CA: ASP), 565
Dey, A., van Breugel, W., Vacca, W. D., et al. 1997, ApJ, 490, 698
Djorgovski, S., Spinrad, H., McCarthy, P., et al. 1988, AJ, 96, 836
Downes, D., & Solomon, P. M. 1998, ApJ, 507, 615
Eales, S. A. 1992, ApJ, 397, 49
Elbaz, D., Jahnke, K., Pantin, E., Le Borgne, D., & Letawe, G. 2009, A&A, 507, 1359
Emonts, B., Carilli, C., Narayanan, D., et al. 2018b, in ASP Conf. Ser. 517, Science with a Next Generation Very Large Array, ed. E. Murphy (San Francisco, CA: ASP), 587
Emonts, B. H. C., De Breuck, C., Lehnert, M. D., et al. 2015b, A&A, 584, A99
Emonts, B. H. C., Lehnert, M. D., Dannerbauer, H., et al. 2018a, MNRAS, 477, L60
Emonts, B. H. C., Lehnert, M. D., Villar-Martín, M., et al. 2016, Sci, 354, 1128
Emonts, B. H. C., Mao, M. Y., Stroe, A., et al. 2015a, MNRAS, 451, 1025
Emonts, B. H. C., Norris, R. P., Feain, I., et al. 2014, MNRAS, 438, 2898
Falkendal, T., De Breuck, C., Lehnert, M. D., et al. 2019, A&A, 621, A27
Falkendal, T., Lehnert, M. D., Vernet, J., et al. 2021, A&A, 645, A120
Fogasy, J., Knudsen, K. K., Drouart, G., & Gullberg, B. 2021, MNRAS, 501, 5973
Fosbury, R. A. E., Morganti, R., Wilson, W., et al. 1998, MNRAS, 296, 701
Fragile, P. C., Anninos, P., Croft, S., et al. 2017, ApJ, 850, 171
Fragile, P. C., Murray, S. D., Anninos, P., & van Breugel, W. 2004, ApJ, 604, 74
Gaibler, V., Khochfar, S., Krause, M., & Silk, J. 2012, MNRAS, 425, 438
Galametz, A., Stern, D., De Breuck, C., et al. 2012, ApJ, 749, 169
Galametz, A., Stern, D., Pentericci, L., et al. 2013, A&A, 559, A2
Genzel, R., Tacconi, L. J., Gracia-Carpio, J., et al. 2010, MNRAS, 407, 2091
Gopal-Krishna, Wiita, P. J. 1991, ApJ, 373, 325
Gullberg, B., De Breuck, C., Lehnert, M. D., et al. 2016a, A&A, 586, A124
Gullberg, B., Lehnert, M. D., De Breuck, C., et al. 2016b, A&A, 591, A73
Hatch, N. A., Overzier, R. A., Röttgering, H. J. A., et al. 2008, MNRAS, 383, 931
Heckman, T. M., Lehnert, M. D., Miley, G. K., & van Breugel, W. 1991, ApJ, 381, 373
Humphrey, A., Villar-Martín, M., Fosbury, R., et al. 2006, MNRAS, 369, 1103
Humphrey, A., Villar-Martín, M., Sánchez, S. F., et al. 2008, MNRAS, 390, 1505
Hunter, T. R., Lucas, R., Broguière, D., et al. 2016, Proc. SPIE, 9914, 99142L
Ivison, R. J., Papadopoulos, P. P., Smail, I., et al. 2011, MNRAS, 412, 1913
Ivison, R. J., Smail, I., Amblard, A., et al. 2012, MNRAS, 425, 1320
Jones, G. C., Maiolino, R., Carniani, S., et al. 2023, MNRAS, 522, 275
Kirkpatrick, C. C., Gitti, M., & Cavagnolo, K. W. 2009, ApJL, 707, L69
Kirkpatrick, C. C., McNamara, B. R., & Cavagnolo, K. W. 2011, ApJL, 731, L23
Klaassen, P. D., Mroczkowski, T. K., Cicone, C., et al. 2020, Proc. SPIE, 11445, 114452F
Klamer, I. J., Ekers, R. D., Sadler, E. M., et al. 2004, ApJL, 612, L97
Klamer, I. J., Ekers, R. D., Sadler, E. M., et al. 2005, ApJL, 621, L1
Kodama, T., Tanaka, I., Kajisawa, M., et al. 2007, MNRAS, 377, 1717
Komissarov, S. S., & Falle, S. A. E. G. 1996, in ASP Conf. Ser. 100, Energy Transport in Radio Galaxies and Quasars, ed. P. E. Hardee, A. H. Bridle, & J. A. Zensus (San Francisco, CA: ASP), 327
Kurk, J. D. 2003, PhD Thesis, Leiden Univ.
Kurk, J. D., Pentericci, L., Röttgering, H. J. A., et al. 2002, RMxAA, 13, 191
Large, M. I., Mills, B. Y., Little, A. G., et al. 1981, MNRAS, 194, 693
Lebowitz, S., Emonts, B., Terndrup, D., et al. 2023, ApJ, 951, 73
Lee, K., Kohno, K., Hatsukade, B., et al. 2023, ApJ, 944, 35
Lehnert, M. D., Heckman, T. M., Chambers, K. C., et al. 1992, ApJ, 393, 68
Li, J., Emonts, B. H. C., Cai, Z., et al. 2021, ApJL, 922, L29
Li, J., Emonts, B. H. C., Cai, Z., et al. 2023, ApJ, 950, 180
Mandal, A., Mukherjee, D., Federrath, C., et al. 2021, MNRAS, 508, 4738
McCarthy, P. J. 1993, ARA&A, 31, 639
McCarthy, P. J., Elston, R., & Eisenhardt, P. 1992, ApJL, 387, L29
McCarthy, P. J., Spinrad, H., Djorgovski, S., et al. 1987a, ApJL, 319, L39
McCarthy, P. J., Spinrad, H., van Breugel, W., et al. 1990, ApJ, 365, 487
McCarthy, P. J., Spinrad, H., & van Breugel, W. 1995, ApJS, 99, 27
McCarthy, P. J., van Breugel, W., Spinrad, H., & Djorgovski, S. 1987b, ApJL, 321, L29
Meenakshi, M., Mukherjee, D., Wagner, A. Y., et al. 2022, MNRAS, 516, 766
Mellema, G., Kurk, J. D., & Röttgering, H. J. A. 2002, A&A, 395, L13
Miley, G. 1980, ARA&A, 18, 165
Miley, G., & De Breuck, C. 2008, A&ARv, 15, 67
Miley, G. K., Overzier, R. A., Zirm, A. W., et al. 2006, ApJL, 650, L29
Morganti, R., Holt, J., Tadhunter, C., et al. 2011, A&A, 535, A97
Morganti, R., Oosterloo, T. A., Tinti, S., et al. 2002, A&A, 387, 830
Murphy, E. 2018, in ASP Conf. Ser. 517, Science with a Next Generation Very Large Array, ed. E. Murphy (San Francisco, CA: ASP), 517
Murthy, S., Morganti, R., Emonts, B., et al. 2020, A&A, 643, A74
Nesvadba, N. P. H., Bicknell, G. V., Mukherjee, D., et al. 2020, A&A, 639, L13
Nesvadba, N. P. H., De Breuck, C., Lehnert, M. D., et al. 2017, A&A, 599, A123
Nesvadba, N. P. H., Neri, R., De Breuck, C., et al. 2009, MNRAS, 395, L16
Overzier, R. A. 2006, PhD Thesis, Leiden University
Overzier, R. A., Harris, D. E., Carilli, C. L., et al. 2005, A&A, 433, 87
Papadopoulos, P. P., Feain, I. J., Wagg, J., & Wilner, D. J. 2008, ApJ, 684, 845
Pentericci, L., McCarthy, P. J., Röttgering, H. J. A., et al. 2001, ApJS, 135, 63
Pentericci, L., Röttgering, H. J. A., Miley, G. K., et al. 1999, A&A, 341, 329
Pentericci, L., Van Reeven, W., Carilli, C. L., et al. 2000, A&AS, 145, 121
Prochaska, J. X., & Hennawi, J. F. 2009, ApJ, 690, 1558
Randall, K. E., Hopkins, A. M., Norris, R. P., et al. 2011, MNRAS, 416, 1135
Rees, M. J. 1989, MNRAS, 239, 1P
Reuland, M., van Breugel, W., de Vries, W., et al. 2007, AJ, 133, 2607
Reuland, M., van Breugel, W., Röttgering, H., et al. 2003, ApJ, 592, 755
Rocca-Volmerange, B., Le Borgne, D., De Breuck, C., et al. 2004, A&A, 415, 931
Roettgering, H. J. A., Lacy, M., Miley, G. K., et al. 1994, A&AS, 108, 79
Roettgering, H. J. A., van Ojik, R., Miley, G. K., et al. 1997, A&A, 326, 505

Salomé, Q., Salomé, P., & Combes, F. 2015, A&A, 574, A34
Saxena, A., Jagannathan, P., Röttgering, H. J. A., et al. 2018, MNRAS, 475, 5041
Seymour, N., Stern, D., De Breuck, C., et al. 2007, ApJS, 171, 353
Smail, I., Scharf, C. A., Ivison, R. J., et al. 2003, ApJ, 599, 86
Solomon, P. M., & Vanden Bout, P. A. 2005, ARA&A, 43, 677
Spinrad, H., Stauffer, J., & Butcher, H. 1981, ApJ, 244, 382
Stern, D., Dey, A., Spinrad, H., et al. 1999, AJ, 117, 1122
Stevens, J. A., Ivison, R. J., Dunlop, J. S., et al. 2003, Natur, 425, 264
Sutherland, R. S., Bicknell, G. V., & Dopita, M. A. 2003, ApJ, 591, 238
Swinbank, A. M., Vernet, J. D. R., Smail, I., et al. 2015, MNRAS, 449, 1298
Tadhunter, C., Holt, J., González Delgado, R., et al. 2011, MNRAS, 412, 960
Tadhunter, C. N., Villar-Martin, M., Morganti, R., et al. 2000, MNRAS, 314, 849
van Breugel, W., Miley, G., Heckman, T., et al. 1985, ApJ, 290, 496
van Ojik, R., Roettgering, H. J. A., Carilli, C. L., et al. 1996, A&A, 313, 25
Venemans, B. P., Röttgering, H. J. A., Miley, G. K., et al. 2007, A&A, 461, 823
Vernet, J., Fosbury, R. A. E., Villar-Martín, M., et al. 2001, A&A, 366, 7
Vernet, J., Lehnert, M. D., De Breuck, C., et al. 2017, A&A, 602, L6
Villar-Martín, M., Emonts, B., Cabrera Lavers, A., et al. 2017, MNRAS, 472, 4659
Villar-Martín, M., Humphrey, A., De Breuck, C., et al. 2007a, MNRAS, 375, 1299
Villar-Martín, M., Sánchez, S. F., De Breuck, C., et al. 2006, MNRAS, 366, L1
Villar-Martín, M., Sánchez, S. F., Humphrey, A., et al. 2007b, MNRAS, 378, 416
Villar-Martín, M., Tadhunter, C., Morganti, R., et al. 1999, MNRAS, 307, 24
Villar-Martín, M., Vernet, J., di Serego Alighieri, S., et al. 2002, MNRAS, 336, 436
Villar-Martín, M., Vernet, J., di Serego Alighieri, S., et al. 2003, MNRAS, 346, 273
Wang, W., Wylezalek, D., De Breuck, C., et al. 2021, A&A, 654, A88
West, M. J. 1994, MNRAS, 268, 79
Wright, E. L. 2006, PASP, 118, 1711
Wylezalek, D., Galametz, A., Stern, D., et al. 2013, ApJ, 769, 79
Zhong, Y., Inoue, A. K., Sugahara, Y., et al. 2023, MNRAS, 522, 6123
Zinn, P.-C., Middelberg, E., Norris, R. P., & Dettmar, R.-J. 2013, ApJ, 774, 66